ChemComm

Unveiling new stable Manganese based photoanode materials via theoretical high-throughput screening and experiments

Journal:	*ChemComm*
Manuscript ID	CC-COM-08-2019-006736.R1
Article Type:	Communication

COMMUNICATION

Unveiling new stable Manganese based photoanode materials via theoretical high-throughput screening and experiments†

Received 00th January 20xx,
Accepted 00th January 20xx

DOI: 10.1039/x0xx00000x

Juhwan Noh ‡[a], Sungwon Kim [a], Geun ho Gu [a], Aniketa Shinde ‡[b], Lan Zhou [b], John M. Gregoire *[b] and Yousung Jung *[a]

With the increasing energy demand, developing renewable fuel production strategies such as photoelectrocatalytic hydrogen production is critical to mitigating global climate chagne. In this work, we experimentally validate a new stable and photoactive material, Mg_2MnO_4, from the exhaustive theoretical exploration of the chemical space of X(=Mg, Ca), Mn and O.

Photo-electro-catalysts that harness solar energy to split water into hydrogen offers a delocalized, clean, and renewable solution to synthesize renewable fuels.[1, 2] Discovering efficient photoelectrocatalyst materials for the oxygen evolution reaction (OER) remains a challenge to realize this technology, and since wide gap semiconductors cannot efficiently utilize the solar spectrum, visible-gap photo-electro-catalysts must be discovered.[3] A large spectrum of semiconductor materials have demonstrated excellent solar absorption and photoactivity,[4-6] but the rapid corrosion of the semiconductor at the solid-electrolyte interface inhibits their application as photo-electro-catalysts.[7, 8] Mn-based oxide materials are satisfactory in this regard, due to their high stability and ability to form a passivation layer under the operating conditions, but few photoactive Mn-based semiconductors have been identified to date.[9, 10] Recently, A. Shinde et al.[11] proposed a material design pipeline combining experimental and theoretical approaches to discover new manganese-based photoanodes by mining the Materials Project database.[12] The proposed approach successfully discovered five new Mn-based oxide materials with great stability, band-gap, and OER activity, motivating the further search beyond the previously reported chemical space of Materials Project (MP) database.[12] Here, we systematically enumerate a large chemical space of Ca-Mn-O and Mg-Mn-O materials (~15,000 materials) and perform the four-tier *ab-initio* screening (see Fig. 1). The screening result is then experimentally synthesized and characterized using combinatorial methods. As a result of the combined theoretical and experimental effort, we report a new photoactive and stable crystal Mg_2MnO_4 under the photo-electro-catalyst operating condition.

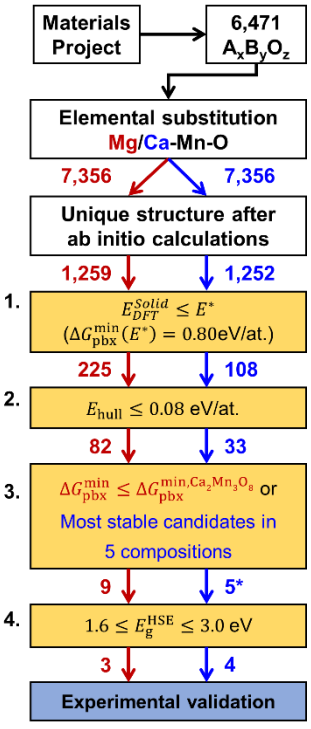

Fig. 1 Four-tier screening employed for discovering new Mn-based oxide photoanode. Bold numbers indicate the number of compounds that meet the screening criteria in the boxes (red for Mg-Mn-O and blue for Ca-Mn-O). Before initiate screening, total ~15,000 materials are enumerated from the Materials Project database where it is reduced to 1,259 and 1,252 unique crystal structure for Mg-Mn-O and Ca-Mn-O, respectively. Tier 1 reduces the chemical space by evaluating a minimum requirement of aqueous state stability (ΔG_{pbx}). At tier 2, experimental synthesizability (or meta-stability) of materials at 0 K and 0 atm is considered. At tier3, to find new materials with improved stability compared to the previously reported most stable materials, $Ca_2Mn_3O_8$, detailed aqueous state stability (ΔG_{pbx}) is analyzed. At the last step, tier 4, the band gap calculated from hybrid density functional is used as criteria which defines the maximum theoretical photo-electro-chemical efficiency. For Ca-Mn-O, no materials meet the ΔG_{pbx} screening criterion, prompting our selection of the 5 materials with the lowest ΔG_{pbx} to consider in subsequent screening steps.

[a] *Department of Chemical and Biomolecular Engineering, Korea Advanced Institute of Science and Technology (KAIST)291 Daehak-ro, Yuseong-gu, Daejeon 34141, Republic of Korea. E-mail: ysjn@kaist.ac.kr*
[b] *Joint Center for Artificial Photosynthesis, California Institute of Technology, Pasadena, CA 91125, USA. E-mail: gregoire@caltech.edu*
† Electronic Supplementary Information (ESI) available: Computational and experimental method and lists of the screened materials.
‡ These authors contributed equally.

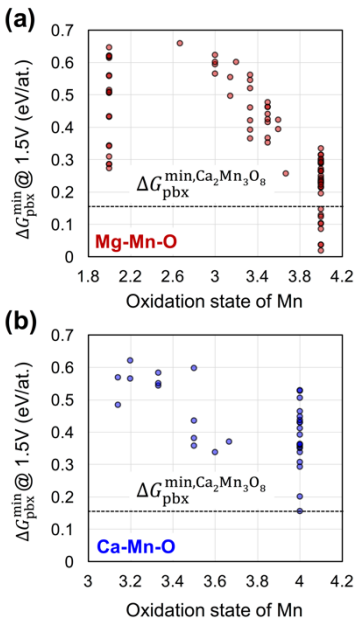

Fig. 2 Minimum Pourbaix stability (ΔG_{pbx}^{min}) at 1.5V vs. RHE over a pH range between 0 and 14 for the (a) 82 Mg-Mn-O materials and (b) 33 Ca-Mn-O materials after passing tier 2. Dashed line indicates ΔG_{pbx}^{min} for the previously reported most stable alkaline-metal-based Mn oxide, $Ca_2Mn_3O_8$.

The screening procedure used in this work is shown in Fig. 1, and the details of the computations and experiments are in Section S1 of Electronic Supplementary Information (ESI). A previous screening study has shown that combining alkaline metal (particularly, Mg, Ca, Sr and Ba) with Mn oxides results in good stability and catalytic activity, the most stable one of which was $Ca_2Mn_3O_8$.[11] However, the screened chemical space was limited to those in the Materials Project database[12] (66 materials for the Mg-Mn-O composition, 73 for Ca-Mn-O, 29 for Ba-Mn-O and 18 for Sr-Mn-O), and an in-depth search could reveal more stable photoanode candidates. Here, we extend it to a hypothetical chemical space of Mg-Mn-O and Ca-Mn-O by creating a larger database by substitution, about 15,000 materials in total. All $A_xB_yO_z$ type ternary oxides from the Materials Project database[12] are first extracted as of August 2018, resulting in a total of 6471 unique crystal structures. Then, A and B are substituted with Mg or Ca and with Mn, respectively, yielding a total of 7,356 alkaline earth manganate structures (see Fig. S4. of ESI for details). We note that the oxidation state of the Mn (OS_{Mn}) is in the reasonable range (between +2 and +4) assuming Ca and Mg are +2 and O is -2.

Before entering tier 1, we first performed the DFT geometry optimizations under the PBE+U functional[13, 14] for the entire dataset defined here, i.e., 7,356 x 2 = 14,712 materials. These enumerated materials then converged to 1,259 and 1,252 unique crystal structures for Mg-Mn-O, and Ca-Mn-O, respectively (see Section S1.1 for computational details). For tier 1 screening, we narrow down the candidates by Gibbs free energy above the Pourbaix hull (ΔG_{pbx}) that represents meta-stability of the given phase in an aqueous electrochemical environment.[15] Here, ΔG_{pbx} is defined as DFT electronic energy (E_{DFT}^{Solid}) above those of the Pourbaix hull at given pH and electrochemical potential.[15] Materials are screened by ΔG_{pbx} which is at least 0.80 eV at 1.5 V vs. RHE and pH between 0 and 14. We define this criterion as E^*. An open-source material analysis code, *Pymatgen* package,[16] is used to calculate the value of E^* under these conditions and are shown in Fig. S5 in the ESI. The potential of 1.5 V vs. RHE is used as it represents the current best OER electrocatalyst with an overpotential of ~ 0.27 V.[17] After these tier 1 DFT calculations of ΔG_{pbx}, a total of 333 unique structures (225 for Mg-Mn-O and 108 for Ca-Mn-O) met the criterion and proceed to the next tier.

To consider the experimental synthesizability (or metastability) of the given materials, in tier 2 we used the energy above the convex hull (E_{hull}) at 0 K and 0 atm, defined as the difference of the thermodynamic formation energy between the given material and the ground state following the approaches used in the MP database.[18, 19] We used the upper bound of the E_{hull} to be 0.080 eV/atom since 80 % of the known meta-stable sulfides and oxides are within this criterion.[20, 21] A total of 115 structures (82 for Mg-Mn-O and 33 for Ca-Mn-O) were yielded (see Fig. S6 in ESI). Because our main objective in this work is to find new stable photoanode materials under reaction condition, in tier 3, we analyzed the detailed aqueous state stability represented by the minimum of Pourbaix hull Gibbs free energy at 1.5 V vs RHE over pH 0-14 range, ΔG_{pbx}^{min}, in Fig. 2 (see Section S5 and S6 of ESI for tabulated E_{hull} and ΔG_{pbx}^{min}). As shown in the Fig. 2, we find that ΔG_{pbx}^{min} is overall inversely proportional to OS_{Mn} for materials with $OS_{Mn} > 2.6$ (except for the Mg-Mn-O with $OS_{Mn} = 2$), indicating that higher OS_{Mn} (i.e. Ca- or Mg-rich state) is a key factor of the electrochemical stability. Thus, materials with Ca/Mg-rich Mn oxide will derive good photo-electrochemical stability under operating conditions. To find new materials with the improved aqueous state stability compared to the previously reported most stable material, $Ca_2Mn_3O_8$ from Materials Project database ($\Delta G_{pbx}^{min,Ca_2Mn_3O_8}$)[11], we compare ΔG_{pbx}^{min} of screened materials with those of $Ca_2Mn_3O_8$, as shown in the Fig. 2. We find nine Mg-Mn-O materials more stable than $Ca_2Mn_3O_8$, but no such Ca-Mn-O materials are found.

Tier 4 considers the band gap of the materials, which defines the maximum theoretical photo-electro-chemical efficiency. We select the screening range of the band gap (E_g^{HSE}) from 1.6 eV to 3.0 eV as suggested by ref.[22] where HSE hybrid functional[23] is used to compute the band gap for the latter 14 materials. A total of seven materials (3 for Mg-Mn-O and 4 for Ca-Mn-O) pass this tier; E_g^{HSE} and ΔG_{pbx}^{min} taken from the tier 3 are shown in the Fig. 3a (see Section S5. and S6. of ESI for all tabulated values). All the identified candidates have OS_{Mn} of 4, which is a common and stable oxidation state of Mn. E_g^{HSE} and ΔG_{pbx}^{min} are shown in Fig. 3a and are consistent with the long-standing observation that there is often a tradeoff wherein a lower band gap energy corresponds to a decrease in stability.[24, 25] In these systems, the higher Mn concentrations and Ca-containing materials have generally lower E_g^{HSE} and higher ΔG_{pbx}^{min} while the lower Mn concentrations and Mg-containing

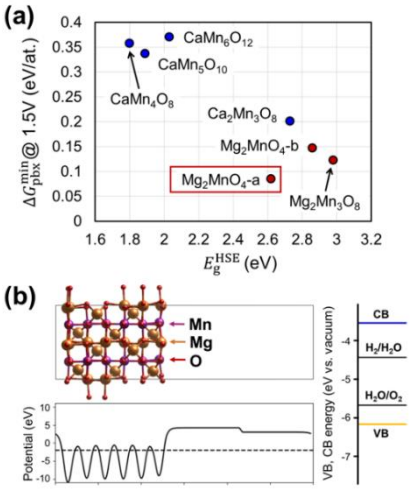

Fig. 3 (a) Promising new photoanode materials identified in this work using high-throughput screening of ~15,000 materials based on the calculated minimum Pourbaix hull Gibbs free energy (ΔG_{pbx}^{min}) at 1.5V with a band gap from hybrid DFT functional (E_g^{HSE}). Red box indicates the experimentally confirmed crystal, Mg_2MnO_4-a. (b) The calculated potential energy (left, solid-line) and band-level alignment for the valence band (VB) and conduction band (CB) relative to the water redox potential (right) for Mg_2MnO_4-a <110> surface. Black dashed line indicates the computed Fermi level.

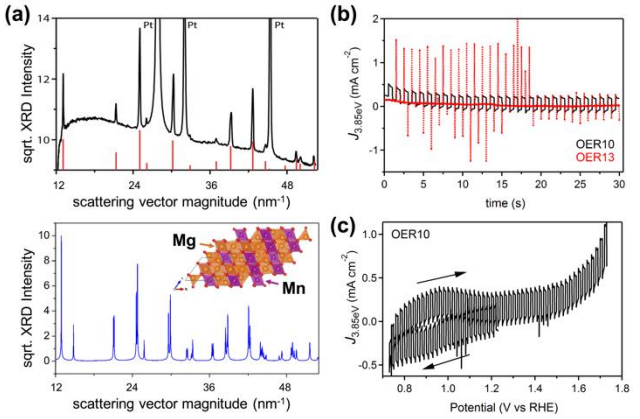

Fig. 4 Crystal structure identifications of the proposed Mg_2MnO_4-a via characterization of $Mg_{0.51}Mn_{0.49}O_z$ thin film, and experimental validation. (a) XRD pattern (black) of the most Mg-rich composition containing phase-pure cubic spinel, which was identified using PDF pattern 19-0773 with a cubic lattice constant of 0.833 nm (red), 0.43% lower than that of the stoichiometric compound. The peaks from the Pt underlayer are also noted. Theoretical XRD pattern (blue) for the proposed Mg_2MnO_4-a was calculated from the PBE+U calculation where its crystal structure is also shown. (b) Chopped-illumination chronoamperometry (385 nm LED) of 2 duplicate samples operated at 1.23 V vs RHE in pH 10 and pH 13 electrolyte, respectively, where sustained photocurrent is only obtained in pH 10 electrolyte. (c) Chopped illumination cyclic voltammogram starting with a cathodic sweep from 1.23 V vs RHE and finishing with an anodic sweep to 1.73 V vs RHE. An anodic photocurrent is observed in each illumination cycle.

materials have higher E_g^{HSE} and lower ΔG_{pbx}^{min}. The most substantial deviation from the general trend is Mg_2MnO_4-a, which is noted in Fig. 3a and exhibits the lowest ΔG_{pbx}^{min} but the median E_g^{HSE}.

In addition, to understand viability of the latter identified Mg_2MnO_4-a, we computed the vacuum-referenced band edge energy level as shown in the Fig. 3b. Following the previous works,[11, 26] the valence band maximum (VBM) and conduction band minimum (CBM) are determined from the most stable surface orientation and termination with the PBE+U functional (see Section S1.3 in ESI for detail). We note that the vacuum level is defined as the potential (ionic plus Hartree) far from the surface, and therefore VBM and CBM are evaluated from the calculated work function and HSE band gap (2.62 eV), respectively. As shown in the Fig. 3b, the <110> surface is found to have the lowest energy, and VBM and CBM are located at 6.17 eV and 3.55 eV below the vacuum level, respectively. The VBM energy is commensurate with the experimental observation of photoactivity for OER, and the band alignment makes Mg_2MnO_4-a a candidate for overall water splitting.

We note that there may exist other metrics (such as photo-electro-chemical experiments for various pH range)[26] to evaluate catalytic activity of photoanode in addition to the stability and band gap indicating that the latter properties can be further added to the future screening pipeline for more complicate and extensive photoanode material design.

The uniqueness of this phase in the computational survey motivated experimental investigation, which proceeded with combinatorial thin film synthesis via physical vapor deposition of an Mg-Mn oxide pseudo-binary composition spread followed by a 3 hour anneal at 850 °C in air. As shown in Fig. 4a, X-ray diffraction (XRD) measurements demonstrate phase-purity of a Mg_2MnO_4-a cubic spinel structure, which is in a good agreement the theoretical XRD as shown in Fig. 4a. We find this structure to be phase pure only at Mn-rich compositions ranging from approximately Mn/(Mn+Mg) = 48% to 62%, where increased Mn alloying corresponds to continuous transformation into the $MgMn_2O_4$ spinel structure. At this composition we instead observe the tetragonal $MgMn_2O_4$, as discussed in further detail in the ESI (Fig. S2). At more Mg-rich compositions, the Mg_6MnO_8 structure is observed. Both Mg_2MnO_4-a and Mg_6MnO_8 are composed of Mg^{+2} and Mn^{+4} and exhibit considerable solubility of Mn^{+2} on Mg^{+2} sites according to XRD. Photo-electrochemical experiments reveal that the mixtures of these phases are photoactive. While the photoactivity at the target composition Mg_2Mn is noteworthy, for the purposes of the present work we focus only on phase-pure materials, prompting our attention to $Mg_{0.51}Mn_{0.49}O_z$ in Fig. 4b and c, the most Mg-rich sample with Mg_2MnO_4-a cubic spinel structure.

The photo-electro-chemical characterization of this sample proceeded using the protocols of ref.[11] An initial test for photoactivity was performed in both pH 10 and pH 13 electrolytes as shown in Fig. 4b. At pH 13, anodic transient currents are observed upon illumination, a clear photoresponse that does not lead to sustained photocurrent. Sustained photocurrent is observed at pH 10, prompting further characterization with a cyclic voltammogram (CV) from 1.23 to 0.73, and to 1.73 V vs RHE as shown in Fig. 4c. The CV reveals an onset of anodic dark current near 1.5 V vs RHE, indicating its excellent catalytic activity for OER in pH 10, in agreement with the previous study of a similar material for electrochemical OER in strong alkaline electrolyte.[27] In addition, an anodic photocurrent is observed in each illumination cycle across the entire potential range as shown in Fig. 4c. Furthermore, the photocurrent does not decrease noticeably with decreasing potential, indicating that the photoanode may have an excellent photovoltage. Measurements at lower potential were not performed due to the electrochemical reduction of Mn^{+4} as discussed previously,[11] which also hampers electrochemical measurement of the flat band potential. The photocurrent at 1.23 V vs. RHE corresponds to an external quantum efficiency of

1.1×10^{-3}, similar to the median value of the five ternary manganate photoanodes discovered via high-throughput computational and experimental screening of Materials Project Database.[11]

X-ray fluorescence (XRF) of the sample in Fig. 4 revealed a metals loading of 20.1 nmol/mm, corresponding to a film thickness of approximately 220 nm. Given the instability of Mg under these electrochemical conditions (Fig. S3)[15], XRF analysis was performed on the sample from Fig. 4b and c before and after (photo)electrochemistry as well as a duplicate sample before and after exposure to the same electrolyte for the same duration but held under open circuit. Results described in the ESI indicate that upon exposure to electrolyte, chemical Mg dissolution results in the formation of a ca. 13 nm MnO_2 passivaiton layer, similar to the self-passivation observed in copper vanadate photoanodes.[8] Some Mn corrosion occurred during the measurements of Fig. 4b and c, and while this corrosion is not enough to strongly impact the observed photoanodic current, study of potential-dependent corrosion and passivation will be required for further development of this photoanode.

In summary, a new oxygen evolution photoanode Mg_2MnO_4 is discovered using the theoretical high-throughput screening and the experimental validations. To explore the larger chemical space than previous studies, we enumerated the chemical space with elemental substitution yielding about 15,000 materials, significantly larger than 139 Mg/Ca-Mn-O materials in Materials Project. Our discovery demonstrates that the extensive search of the promising elemental combinations can lead to active materials discovery from the omitted chemical space.

The theoretical screening work was supported by Korea Institute of Energy Technology Evaluation and Planning (KETEP-20188500000440), and the experimental work was supported by U.S. Department of Energy (DOE) under Award Number DE-SC0004993.

Conflicts of interest

There are no conflicts to declare.

Notes and references

1. J. Schneider, D. Bahnemann, J. Ye, G. L. Puma and D. D. Dionysiou, *Photocatalysis: fundamentals and perspectives*, Royal Society of Chemistry, 2016.
2. D. K. Lee, D. Lee, M. A. Lumley and K.-S. Choi, *Chemical Society Reviews*, 2019.
3. M. Woodhouse and B. A. Parkinson, *Chemistry of Materials*, 2008, **20**, 2495-2502.
4. V. Stevanović, S. Lany, D. S. Ginley, W. Tumas and A. Zunger, *Physical Chemistry Chemical Physics*, 2014, **16**, 3706-3714.
5. D. Guevarra, A. Shinde, S. Suram, I. Sharp, F. Toma, J. Haber and J. Gregoire, *Energy & Environmental Science*, 2016, **9**, 565-580.
6. C. Zachäus, F. F. Abdi, L. M. Peter and R. Van De Krol, *Chemical science*, 2017, **8**, 3712-3719.
7. S. Hu, M. R. Shaner, J. A. Beardslee, M. Lichterman, B. S. Brunschwig and N. S. Lewis, *Science*, 2014, **344**, 1005-1009.
8. L. Zhou, Q. Yan, J. Yu, R. J. Jones, N. Becerra-Stasiewicz, S. K. Suram, A. Shinde, D. Guevarra, J. B. Neaton and K. A. Persson, *Physical Chemistry Chemical Physics*, 2016, **18**, 9349-9352.
9. K. N. Ferreira, T. M. Iverson, K. Maghlaoui, J. Barber and S. Iwata, *Science*, 2004, **303**, 1831-1838.
10. M. M. Najafpour, G. Renger, M. Hołyńska, A. N. Moghaddam, E.-M. Aro, R. Carpentier, H. Nishihara, J. J. Eaton-Rye, J.-R. Shen and S. I. Allakhverdiev, *Chemical reviews*, 2016, **116**, 2886-2936.
11. A. Shinde, S. K. Suram, Q. Yan, L. Zhou, A. K. Singh, J. Yu, K. A. Persson, J. B. Neaton and J. M. Gregoire, *ACS Energy Letters*, 2017, **2**, 2307-2312.
12. A. Jain, S. P. Ong, G. Hautier, W. Chen, W. D. Richards, S. Dacek, S. Cholia, D. Gunter, D. Skinner and G. Ceder, *Apl Materials*, 2013, **1**, 011002.
13. J. P. Perdew, K. Burke and M. Ernzerhof, *Physical review letters*, 1996, **77**, 3865.
14. V. I. Anisimov, F. Aryasetiawan and A. Lichtenstein, *Journal of Physics: Condensed Matter*, 1997, **9**, 767.
15. A. K. Singh, L. Zhou, A. Shinde, S. K. Suram, J. H. Montoya, D. Winston, J. M. Gregoire and K. A. Persson, *Chemistry of Materials*, 2017, **29**, 10159-10167.
16. S. P. Ong, W. D. Richards, A. Jain, G. Hautier, M. Kocher, S. Cholia, D. Gunter, V. L. Chevrier, K. A. Persson and G. Ceder, *Computational Materials Science*, 2013, **68**, 314-319.
17. M. Tahir, L. Pan, F. Idrees, X. Zhang, L. Wang, J.-J. Zou and Z. L. Wang, *Nano Energy*, 2017, **37**, 136-157.
18. L. Wang, T. Maxisch and G. Ceder, *Physical Review B*, 2006, **73**, 195107.
19. A. Jain, G. Hautier, S. P. Ong, C. J. Moore, C. C. Fischer, K. A. Persson and G. Ceder, *Physical Review B*, 2011, **84**, 045115.
20. M. Aykol, S. S. Dwaraknath, W. Sun and K. A. Persson, *Science advances*, 2018, **4**, eaaq0148.
21. A. K. Singh, J. H. Montoya, J. M. Gregoire and K. A. Persson, *Nat Commun*, 2019, **10**, 443.
22. K. T. Fountaine, H. J. Lewerenz and H. A. Atwater, *Nature communications*, 2016, **7**, 13706.
23. J. Heyd, G. E. Scuseria and M. Ernzerhof, *The Journal of chemical physics*, 2003, **118**, 8207-8215.
24. A. J. Bard and M. S. Wrighton, *Journal of the Electrochemical Society*, 1977, **124**, 1706-1710.
25. H. Gerischer, *Journal of Electroanalytical Chemistry and Interfacial Electrochemistry*, 1977, **82**, 133-143.
26. Q. Yan, J. Yu, S. K. Suram, L. Zhou, A. Shinde, P. F. Newhouse, W. Chen, G. Li, K. A. Persson and J. M. Gregoire, *Proceedings of the National Academy of Sciences*, 2017, **114**, 3040-3043.
27. N. Garg, K. V. Ramanujachary, S. E. Lofland and A. K. Ganguli, *Journal of Solid State Chemistry*, 2013, **197**, 392-397.